iSense: Intelligent Object Sensing and Robot Tracking Through Networked Coupled Magnetic Resonant Coils

Kai Li, *Student Member, IEEE*, Ufuk Muncuk, M. Yousof Naderi, and Kaushik R. Chowdhury, *Senior Member, IEEE*

***Abstract*—Object sensing and tracking using electric and magnetic fields allow intelligent interaction, automation, and adaptation in cyber–physical systems. Our approach, called iSense, uses a software-defined collaborative sensing technique for the detection of the type of object when placed on a large surface and tracking its mobility. iSense is cost effective, low power, and scalable, which allows its use over large surfaces. First, we introduce a dual-coil magnetic resonant sensing architecture based on nested coils, i.e., passive (outer) and active (inner) coils, for low-power contactless sensing. Second, a data-driven support vector machine-based approach helps to classify different types of objects using the voltage readings obtained at the passive coil. iSense combines sensed voltage information from multiple different coils spread over the surface with a group-based interference mitigation mechanism between coils for collaborative sensing. We validate our system with real-time prototype and experimental evaluations. We demonstrate the detection of seven different types of objects over three different materials, and real-time detection and tracking of mobile objects including a robot car. Experimental results show that each sensing coil only consumes few milliwatts, i.e., 18× less than inductive sensing and 15× less than classical magnetic resonance sensing, extend sensing depth to 3 cm, and enable tracking on the large surface sensing with more than 90% accuracy for velocity estimation.**

***Index Terms*—Contactless sensing, magnetic resonance, mobile car tracking, object detection and classification.**

I. INTRODUCTION

OBJECT detection and tracking based on both far and near electromagnetic fields have been studied extensively over the past several years. While great strides have been made, existing solutions have several limitations: radio-frequency (RF)-based far-field sensing solutions require specialized circuits and antenna design, with the risk of consuming high power at the transmitter. Though RF energy harvesting [1] can be used in short-range sensing for IoT [2]–[5] sensor, other wireless localization solutions based on reflected RF signals from Bluetooth, ZigBee, RFID [6], [7], Wi-Fi [8], UWB radios [9], and backscatter [10], [11] require a second (receiver) device and/or additional signal reflectors to send feedback to the transmitter side to estimate the channel state. State-of-the-art near-field magnetic induction-based sensing solutions, such as the analog and digital sensing in Qi [12], are limited in distance to few mm but also requires perfect alignment between the sensing coil and the object. Industry standard Qi solutions today allow one object sensing per coil and incur a power cost of (1/3) W per coil, which makes it costly and complex to scale over a large area. Other low-cost sensing solutions, such as resistive sensing [13], [14] and capacitive coupling [15], [16] are not capable of sensing materials other than low-conductive objects. The proposed iSense system in this article enables the detection and tracking of electronic devices without requirements of conventional sensing technologies, such as the need for an attachment or integration of an additional receiver coil or circuit in the target electronic device, line-of-sight requirement between the sensor and the electronic device, and specific ranges of temperatures at the target device. Some iSense applications include sensing and tracking electronic devices over the surface, robot tracking, foreign object detection for wireless charging [17]–[22], drone sensing to facilitate precise landing, and smart homes with intelligent surfaces.

A. *iSense Operational Overview*[1]

Fig. 1 depicts an overview of our system architecture and components. Each node consists of an active coil, a passive coil, a sensing circuit, transceiver, and a software controller. The inner smaller coil is connected to the continuous-wave generator, and the outer bigger coil acts a passive coil. The coils are so designed such that they are in resonance with each other, when there is active current in the smaller coil and no object is placed on the surface. Thus, the passive coil acts a resonator relay that extends the magnetic field generated by the current with extremely low-power consumption. Each such dual-coil sensing element (henceforth called as a *node*) operates in the kHz band. The coils are networked together and exchange control messages with the network controller.

Manuscript received September 23, 2020; revised December 10, 2020; accepted January 6, 2021. Date of publication January 22, 2021; date of current version April 7, 2021. This work was supported by the funds available through the U.S. National Science Foundation under Award CNS 1452628. *(Corresponding author: Kai Li.)*

The authors are with the Department of Electrical and Computer Engineering, Northeastern University, Boston, MA 02120 USA (e-mail: likai2@coe.neu.edu; umuncuk@coe.neu.edu; naderi@ece.neu.edu; krc@ece.neu.edu).

Digital Object Identifier 10.1109/JIOT.2021.3053632

[1]An earlier version of this article [23] was presented at the 2019 IEEE Global Communications Conference (GLOBECOM), and received the Best Paper Award for the "SAC-IoT" Track. DOI: 10.1109/GLOBECOM38437.2019.9013158.

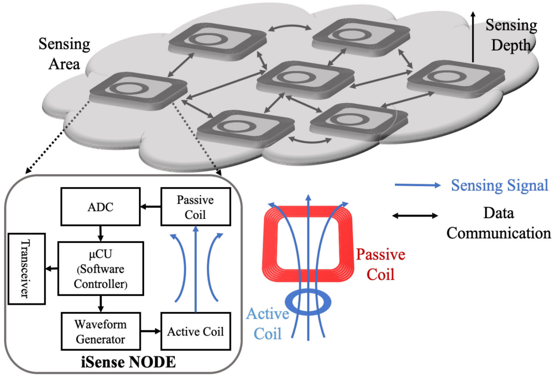

Fig. 1. System overview of iSense nodes and network with low-power-distributed sensing over surface and distance.

Multiple *nodes* are attached to the underside of a large surface such as a desk, and as long as the separation width between the sensing object and the node array is less than 3 cm, iSense can operate with high accuracy. When an object is placed on the surface, each node measures the induced voltage in the outer coil and reports back these measurements to the central controller. Similarly, if the object moves, the nodes detect similar changes and transmit update messages to the controller. The central controller fuses all the measurement data reported by the entire node array and matches the voltage patterns.

B. iSense Design Challenges

Regardless of the design and sensing technology, the dimensions of the coils influence majorly the performance of sensing. For sensing with low-power consumption (in range of mW), both inductive and magnetic resonance-based approaches provide only mm-scale sensing distance. Additionally, to cover a large area, solutions, such as increasing the size of the sensing coil, using 1–1 proportion of coils per charging location, increase system cost and overall power consumption exponentially. Furthermore, measurements by a given coil can result in missed detection. For example, consider the two object placement scenarios below that excite the coil to similar extents: 1) an object with a size bigger than the sensing coil and 2) a larger object that covers multiple coils but with a partial coverage of each sensing coil, and a smaller object that covers part of only one sensing coil. Both situations give rise to similar voltage changes from the partially covered sensing coil. To address these challenges, we design a system that takes into consideration input data from multiple coils at the same time. Thus, there is a need for systematic measurements and algorithms to distinguish between voltage changes for different types of objects. Another design challenge is the interference between neighbor sensing coils. The interference caused by mutual coupling between neighbor coils can distort sensor voltage readings (e.g., unexpected fluctuations on sensing data) and results in inaccurate object localization and tracking. In order to address this challenge, we design a unique interference mitigation method based on the grouping of the coils, where each group has a different coil size.

C. Contributions

The main contributions of iSense can be summarized in terms of hardware and software as follows.

1) We design a dual-coil sensing architecture that enables low-power contactless sensing. It extends the effective sensing distance $5\times$ times compared to the current state-of-the-art coil sensing solutions such as Qi, and sensing coverage $4\times$ times compared to a single coil configuration at $18\times$ energy savings.
2) We provide the theoretical framework along COMSOL Multiphysics simulations for our sensing design.
3) We conduct a set of experiments and demonstrate accurate detection of different objects over distance through software-based detection of voltage changes and object area coverage.
4) We propose a multicoil voltage gradient tracking method that can localize and track object motion over the surface.
5) We design and build a group-based interference mitigation scheme based on dividing the sensing coils into two groups, where each group has a different coil size and coils are arranged to work together without interference for collaborative sensing. This configuration can properly mitigate the interference by reducing the mutual coupling between nearby coils.
6) We build a prototype that consists of a sensing node with a software controller. We then deploy a node array under different surface materials to demonstrate real-time sensing over a large surface area.
7) We experimentally demonstrate a demo for the localization and tracking of a mobile car and devise a car speed velocity estimation approach based on multicoils voltage readings.

This article is organized as follows. In Section II, we review the existing works related to wireless localization and tracking of objects. Section III discusses the iSense system design and theoretical analysis. iSense hardware implementation is described in Section IV. Section V demonstrates the iSense experimental results. Section VI studies sensing, localization, and tracking for the application of a mobile robot car. Section VII presents the conclusions and future works.

II. Related Work

Localization and tracking solutions based on the reflected RF signals from technologies, such as WiFi, Bluetooth, ZigBee, LoRa, and RFID have been extensively studied [9], [24]. However: 1) multipath reflections from the environment; 2) need for a receiver device and/or additional signal reflectors; and 3) complex and power consuming algorithms at the transmitter are the main shortcomings of these works. Recent advancements in smartphones wireless charging have popularized coil-based object sensing, such as inductive-based backscatter [12]. However, coils need to be perfectly aligned and separated by less than 7 mm between receiver and transmitter. Magnetic MIMO [25], analogous to the concept of MIMO in RF signals, uses six power amplifiers to deliver power to a phone through a table. This uses the current

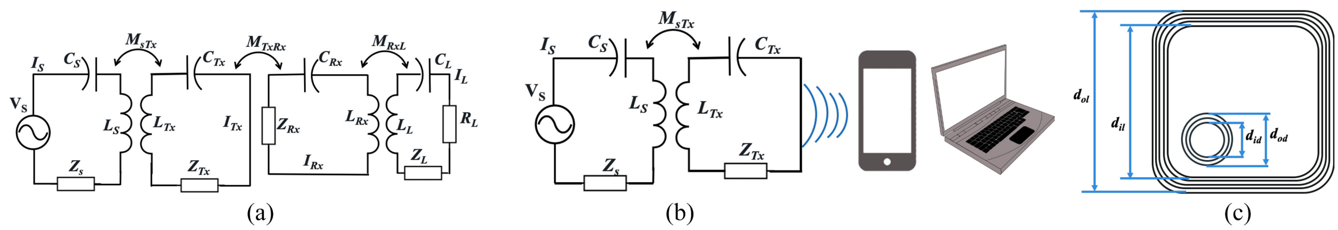

Fig. 2. Circuit schematics of (a) strongly coupled resonant wireless power transfer, (b) proposed dual-coil contactless magnetic object sensing, and (c) dual-coil architecture with active inner and passive outer coils.

change from each coil as the feedback to localize the position of a given phone and then controls the current of each amplifier to beamform the power to the receiver. While the receiver does not need perfect alignment with the transmitter, each coil needs one amplifier, which drives up cost. Second, the current feedback induced from the mutual coupling between the transmitter and receiver prolongs sensing time. Both the inductive coupling backscatter method and the magnetic resonant current sensing method need an additional coil inside the object, which limits the application of the sensing system. The contactless sensing system in iSense is motivated by the need to simplify sensing, increase the sensing distance and area, and provide flexibility as we do not need extra coils or circuits in the target object.

III. System Design and Theoretical Analysis

A. *Magnetic Dual-Coil Contact-Less Sensing*

The concept of strongly coupled magnetic resonance used in iSense is based on the coupled mode theory, which is utilized in the wireless power transfer [26]. This approach significantly extends the charging distance compared to the traditional 1:1 transmitter–receiver magnetic resonance or inductive charging.

Fig. 2(a) shows the circuits for strongly coupled magnetic resonance power transfer, where the source coil connects to the ac power source and generates the magnetic field. The oscillating magnetic field resonates in the transmitter coil. On the other side, the magnetic field from the transmitter is converted into the current in the receiver coil. This current creates a secondary magnetic field within the load coil. This field energy is converted into the current within the device represented as R_l. Fig. 2(b) shows the circuit schematic of our design and Fig. 2(c) shows its architecture with the two coils. Different from the wireless power transfer, in the iSense magnetic contactless sensing system, the objects do not have a receiver coil inside. Various objects with relative high conductive materials, such as cell phone, laptop, and mouse change the magnetic field distribution at the transmitter outer coil. This effect can be measured via voltage changes in the outer coil. The amount of change depends on multiple variables, such as size, shape, materials, magnetic permeability, electrical conductivity, and the overlapping area between object and the coil.

Next, we detail the theory behind strongly coupled resonant wireless transfer and accordingly introduce our object sensing analytical approach. Table I summarizes the circuit parameters used in our formulations. We assume the self-inductance, impedance, mutual inductance, resistance, and angular frequency of input ac signal are given, as they depend on characteristics of the hardware and coils. Then, by using Kirchhoff's laws, we calculate the induced currents at the source, Tx, Rx, and load coils, as shown in Fig. 2(a)

TABLE I
Summary Description Symbols in Circuit Equations

Symbol	Description
V_s	Input AC signal voltage at source coil
I_s	Current amplitude at source coil
C_s	Capacitance at source coil
L_s	Self inductance at source coil
M_{sTx}	Mutual inductance between source and Tx
Z_s	Resistance of input AC signal at source coil circuit
I_{Tx}	Current amplitude at Tx coil
L_{Tx}	Self inductance at Tx coil
C_{Tx}	Capacitance at Tx coil
Z_{Tx}	Impedance of Tx circuit
M_{TxRx}	Mutual inductance between Tx and Rx
I_{Rx}	Current amplitude at Rx coil
L_{Rx}	Self inductance at Rx coil
C_{Rx}	Capacitance at Rx coil
Z_{Rx}	Impedance of Rx circuit
M_{RxL}	Mutual inductance between Rx and load
I_L	Current amplitude at load coil
L_L	Self inductance at load coil
C_L	Capacitance at load coil
R_L	Resistance of load coil
Z_{LTx}	Impedance of Tx coil
Z_{CTx}	Impedance of capacitor at Tx circuit
ω	Angular Frequency of AC source

$$V_s = I_s(j\omega L_s + \frac{1}{j\omega C_s} + Z_s) - j\omega M_{sTx} I_L \tag{1}$$

$$I_{T_x}(j\omega L_{T_x} + \frac{1}{j\omega C_{T_x}} + Z_{T_x}) + j\omega(M_{sTx} I_s - M_{TxRx} I_{R_x}) = 0 \tag{2}$$

$$I_{R_x}(j\omega L_{R_x} + \frac{1}{j\omega C_{R_x}} + Z_{R_x}) + j\omega(M_{RxL} I_L - M_{TxRx} I_{T_x}) = 0 \tag{3}$$

$$I_L(j\omega L_L + \frac{1}{j\omega C_L} + Z_L + R_L) + j\omega M_{RxL} I_s = 0. \tag{4}$$

In the case of the magnetic dual-coil object sensing from Fig. 2(b), both Rx and load coils are replaced by the object. Recall that the source coil is the smaller inner coil and the passive coil is the larger outer coil. Accordingly, the circuit equations for the dual-coil system can be explained by the following equations:

$$V_s = I_s(j\omega L_s + \frac{1}{j\omega C_s} + Z_s) - j\omega M_{sTx} I_{Tx} \tag{5}$$

$$I_{T_x}(j\omega L_{T_x} + \frac{1}{j\omega C_{T_x}} + Z_{T_x}) + j\omega M_{sTx} I_s = 0 \tag{6}$$

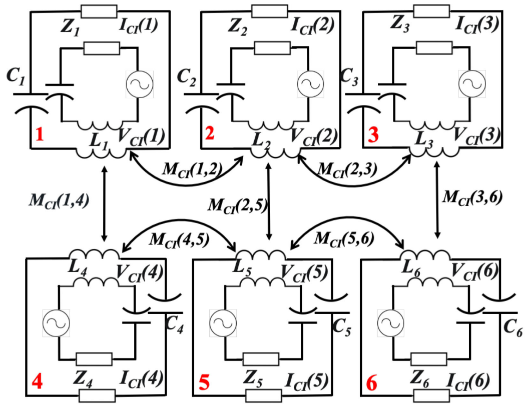

Fig. 3. Circuit diagram of a large surface with multiple sensing coil unit.

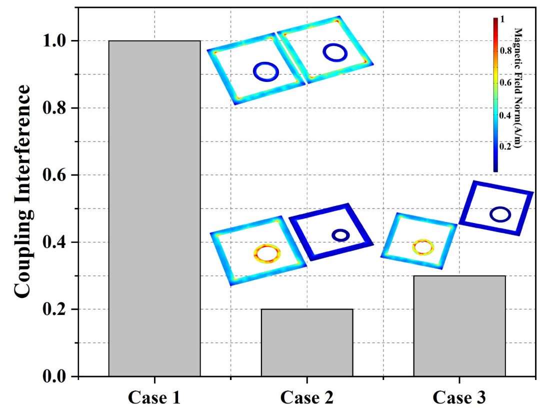

Fig. 4. Normalized coupling between two coils for three positioning cases.

$$Z_{Tx} = Z_{LTx} + Z_{CTx}. \tag{7}$$

Here, the change of the current amplitude at the transmitter outer coil is negligible because the ac power of inner source coil is very low (mW). At resonant mode, $j\omega L_{Tx}$ and $j\omega C_{Tx}$ cancel each other. V_{Tx} is the voltage of outer coil when there is no object and can be calculated as follows:

$$V_{Tx} = j\omega M_{sTx} I_s \tag{8}$$

$$V_{Tx} = I_{Tx}\ Z_{Tx} = I_{Tx}\ (Z_{LTx} + Z_{CTx}). \tag{9}$$

Once an object comes within sensing coverage and distance, the impedance of the outer coil Z_{LTx} changes to Z'_{LTx} and, accordingly, the voltage change at the outer coil is calculated as

$$|\Delta V| = \left| I_{Tx}(Z'_{LTx} - Z_{LTx}) \right|. \tag{10}$$

B. Group-Based Coupling Interference Mitigation

The key challenge in designing a reliable and accurate sensing and tracking system based on the networked coils is to have consistent sensing readings. However, the mutual inductance coupling between neighboring coils can create a random interference on the magnetic field, and causes undesired fluctuations on the voltage change at the output of passive coils. We call this *coupling interference* that impacts negatively the performance and accuracy of object sensing and tracking.

Fig. 3 shows the case of multirow networked coils. The induced current at each outer coil n is generated by its inner coil mutual coupling $M_{STx}(n)$ and coupling interference from all of its neighbors $M_{CI}(n, m)$, where m is the immediate neighbors of coil n. We consider the current that is created by the total sum of coupling interference on outer coil n as $I_{CI}(n)$. The coupling interference can be removed by minimizing the amplitude of the current. The circuit equation between neighbor coil 1 (n = 1) and coil 2 (m = 2) based on Kirchhoff's laws is expressed as follows:

$$I_{CI}(1)(j\omega L_1 + \frac{1}{j\omega C_1} + Z_1) + j\omega M_{CI}(1,2) I_{CI}(2) = 0 \tag{11}$$

$$I_{CI}(2)(j\omega L_2 + \frac{1}{j\omega C_2} + Z_2) + j\omega M_{CI}(1,2) I_{CI}(1) = 0 \tag{12}$$

$$M_{CI}(1,2) = k_{CI}\sqrt{L_1 L_2} \tag{13}$$

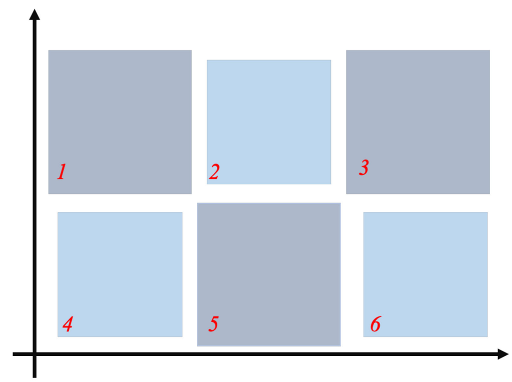

Fig. 5. Size-based grouping of sensing coils for coupling interference mitigation.

where k_{CI} is the coupling coefficient between the two coils. In the calculation of mutual inductance [27]–[29], the inductance decreases dramatically with an increase in the distance and the size ratio of two coils. For example, [27], [28] reported 80% amplitude drop with cm coil separation, and [27] reported on 90% drop when ratio of the size ratio of two coils becomes six.

Next, we provide our evaluation results on the impacts of the relative size and position on the coupling of neighbor coils. In particular, two neighbor coils in a multirow networked coils could have three main cases based on their size and position: 1) case 1 is two identical coils with vertical edge-by-edge position such as coils one and four or horizontally edge-by-edge position such as coils one and two in Fig. 3; 2) case 2 is the same relative edge-to-edge coils position as case 1, but with different coil size; and 3) case 3 is two identical coils, but in diagonal position relative to each other such as coils one and five or two and four in Fig. 3. Fig. 4 demonstrates the normalized coupling results for these cases based on the magnetic field distribution obtained in COMSOL Multiphysics [30]. The results show the strong coupling interference for case 1, and significant drop of more than 80% for the case 2, where we have two coil sizes 12 and 14.5 cm. Furthermore, the coupling has been dropped more than 70% in the case of the identical coils with diagonal position. Accordingly, we design a coupling interference mitigation approach with sensing coils

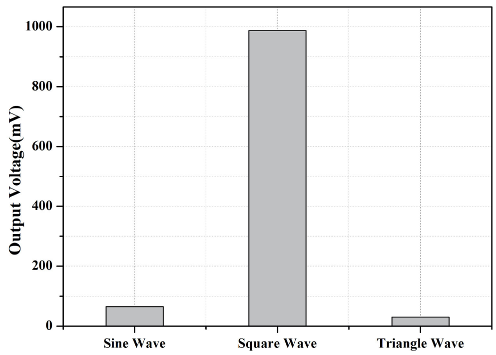

Fig. 6. Measured output voltage of the outer coil (mV).

have been divided into two groups based on their sizes and placed alternatively next to each other. Fig. 5 shows an example arrangement, where group one is the larger coil size and group two is the smaller coil size.

C. Waveform Design and Analysis

As described in the previous section, an ac square wave signal is used to generate an oscillating magnetic field for sensing. This section first experimentally compares the sensing output voltage for three different waveforms: 1) sine; 2) square; and 3) triangle waves, and then demonstrates the impact of offset value and duty cycle of the ac square wave on the sensing performance.

We first conduct the experiment with different waveforms with coil size 12 cm $\times$ 12 cm. In the experiment, the wave generator is an Analog Discovery [31]. With waveform being the only variable, the rest of the parameters of each input signal are the same; the peak–peak amplitude is 5 V, frequency is 200 kHz, offset is 0 V, and duty cycle is 50%.

The output voltages of the outer coil for different waveforms are shown in Fig. 6. We see that the square wave provides the largest output voltage, then sine wave, and the smallest voltage is for triangle wave. The higher the output voltage readings, the higher is the accuracy and larger sensing distance for object detection and tracking. In particular, the square waves generate the strongest magnetic field compared to sine and triangle waves for the same input power. In the frequency domain, a square wave comprises of the summation of an infinite number of harmonic sine waves. Each harmonic generates their own magnetic field and the summation of all field is larger than the field generated by a single sine or triangle wave. Additionally, the square wave generates a peak current for a longer amount of time than a sine or triangle wave, since square wave has stable peak in every time period of one wavelength. However, as the voltage value changes from 0 to peak value for sine and triangle waves in every time period of one wavelength, this results in a lower induced current in the coil compared with the square wave.

Next, we show the results of different offset values on the sensing performance. A square waveform with offset 0 V is shown in Fig. 7(a). Here, the peak-peak voltage is set as 5 V and the frequency is 200kHz. Fig. 7(b) shows the experimental results for different offset values, from 0 V to 5 V

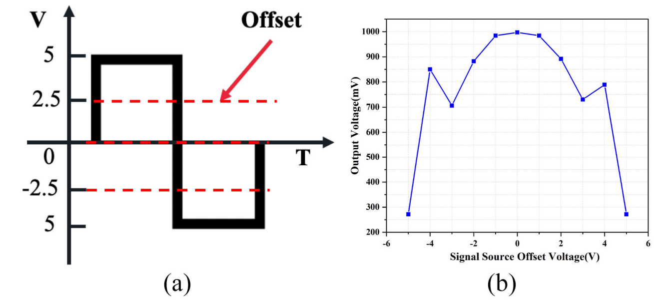

Fig. 7. Offset value of (a) square wave signal and (b) output voltage amplitude of sensing results.

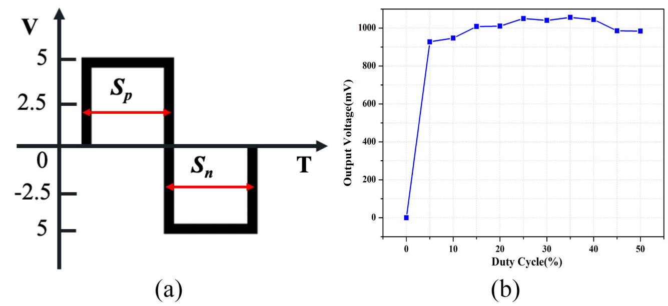

Fig. 8. Duty cycle value of (a) square wave signal and (b) output voltage amplitude of sensing results.

and -5 V to 0 V with 1 V intervals. In this experiment, the offset value is either positive or negative, and the peak-peak value is unchanged. It is observed that the output value change is monotonous to the change offset value. Furthermore, the sensing output voltage is maximum at zero voltage offset.

Fig. 8(a) depicts the duration of positive and negative parts of a square wave as S_p and S_n, where we define duty cycle ratio as $[S_p/(S_p + S_n)]$. The duty cycle can range from 0% to 50%. Fig. 8(b) show the correlations between different duty cycle ratios and the output sensing value. One can see that the output voltage becomes stable while the duty cycle is greater than 15%. From the hardware implementation view, a square wave signal generator with 50% duty cycle does not require phase shifters and timer, and is more cost-effective.

D. Sensing Field Simulation Analysis

We use COMSOL Multiphysics [30] to study and visualize the magnetic field and impedance changes due to presence of objects.

Fig. 9 depicts the magnetic field, where the red arrow represents the direction and the relative amplitude of magnetic field. We used the same coil design parameters as used in our experimental setup (Section V) in terms of the number of turns, dimension of inner and outer coils, and the relative position between the outer coil, and the inner coil. We use 200-kHz square wave signal with amplitude 1 as a current source to power up the inner coil and generate an oscillating magnetic field. At the outer coil, we place a capacitor in serial with the outer coil and calculate its self inductance. Fig. 9(a) presents the magnetic field distribution for the case of no object presence and Fig. 9(b) shows the case that an object is present. It

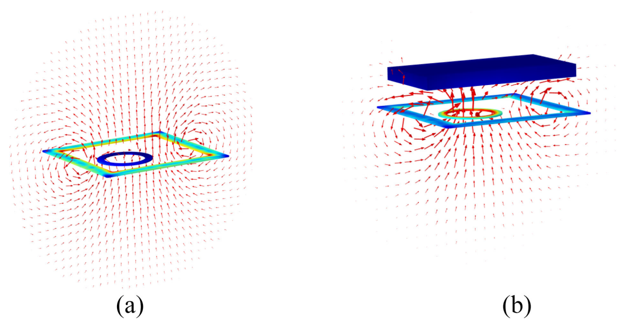

Fig. 9. Simulation results of magnetic field change between two cases: (a) object is not nearby and (b) object is nearby.

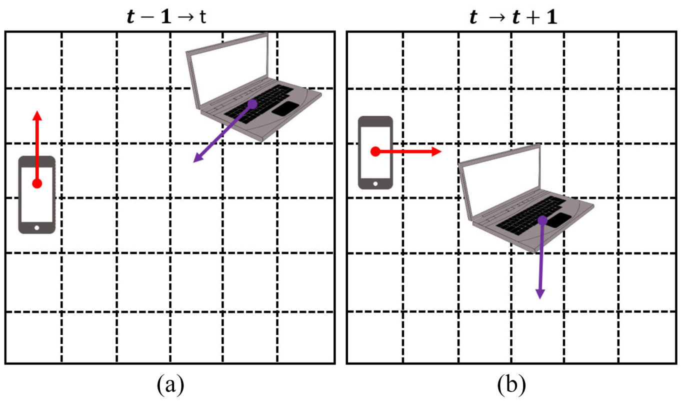

Fig. 10. Multicoil network, where each square block denotes a sensing node. Objects transition around the surface (a) from time $t-1$ to t and (b) from t to $t+1$.

can observed that the object changes the magnetic field distribution around the two coils, and the impedance Z_{LTx} changes from 2.8310 ohms to 0.8 ohm. This impedance change is performed as the voltage change of the outer coil. Next, we will theoretically analyze multicoil object detection classification and tracking.

E. MultiCoil Object Detection, Classification, and Tracking

In this section, we extend iSense to object classification and tracking. While voltage readings in an individual coil can detect the presence of an object, they cannot accurately predict the type of objects. Additionally, an individual coil is not capable of tracking an object over an area. For example, objects with different sizes and types but the same overlapping coverage with a sensing node can cause a similar extent of voltage changes. To address these challenges and enable object tracking, we take into consideration readings from multiple coils at the same time. Accordingly, we propose and build a network of coils with a software controller and a method of collaborative sensing and tracking.

Fig. 10 shows the idea of a multicoil network, where each square block is an iSense node. As we see, $m \times k$ nodes cover a large surface area.

Object Detection: To detect the presence of an object, each node senses individually within its sensing coverage and shares voltage changes via the update messages to the central controller. In our current implementation, each iSense node senses

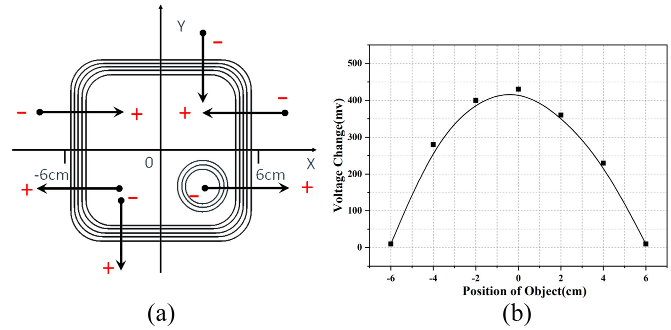

Fig. 11. Positive and negative voltage changes of a moving object (a) along the x-and y-axes of the sensing coil and (b) as a function of the distance from the coil center.

at an interval of 20 ms, and averages every 50 samples to get the latest sensed voltage. At time t, a *voltage matrix* of the sensing surface can be computed as follows:

$$V(t) = \begin{bmatrix} V_{11} & V_{12} & \dots & V_{1k} \\ V_{21} & V_{22} & \dots & V_{2k} \\ \vdots & \vdots & \ddots & \vdots \\ V_{m1} & V_{m2} & \dots & V_{mk} \end{bmatrix} \tag{14}$$

where V_{ij} denotes the sensed voltage of the node located at position (i, j). Regardless of the type and size of the object, any sensed voltage higher than a given noise threshold (i.e., empirically determined based on experiments) indicates the presence of an object. Additionally, based on the voltage matrix, we can detect the presence of multiple objects over the surface and their positions, when V_{ij} is greater than the noise threshold.

Object Classification: After object detection, we need to identify the type of each object, for which we leverage a support vector machine (SVM) classifier. In particular, we divide our experimental data into a training and a testing set in a 4:1 ratio, i.e., for each object, out of five experiments, four are used for training and one is used for testing. A multicoil network can have sensing nodes with one group or two groups configuration. In one group configuration, all coils have the same size, and in two groups configuration group one consists of sensing nodes with coil size S_{G1} and group two consists of nodes with coil size S_{G2}. Matrix S with $m \times k$ elements determine the coils layout configuration, where each element (i, j) in S indicates the size of sensing coil for sensing node (i, j). The experimental data need to be collected separately for each coils layout configuration. Furthermore, the voltage matrix measurements are collected for each object when placed on all node positions on a given coils configuration. The voltage matrix provides information about the voltage change values, the locations of covered nodes, and the number of covered nodes. Our feature vector consists of: 1) coils layout configuration; 2) range of possible sensed voltages; 3) number of covered nodes; and 4) locations of covered blocks. Depending on the overlapping area between an object and sensing coil, the value of voltage change lies within a range, as an example shown in Fig. 11. For a given coil configuration, we collect sensing data for possible overlapping areas of an object and use the voltage range as our SVM feature. It is possible that an object may cover one or more sensing nodes. We also consider this scenario and the numbers of covered nodes by each object as an SVM feature in type classification. The coil layout configuration and locations of covered blocks as input features in training data capture the location and type of sensing coils in the device-type classification process. Additionally, since iSense has been trained with data of a device located at different node positions on the surface, it can differentiate over different object locations in real-time based on the locations of covered nodes and voltage change. It is noteworthy that the device type detection depends on the collected training data for the device hardware, and SVM will detect the type of hardware that the classifier has been trained before.

Object Mobility Tracking: Our collaborative tracking method first computes the voltage gradient matrix and then estimates the motion and direction of multiple moving objects through signs of ΔV elements in voltage gradient matrices. This voltage gradient matrix between time $t-1$ and t is defined as

$$\Delta V(t-1,t) = \begin{bmatrix} \Delta V_{11}^{t} & \dots & \Delta V_{1p}^{t} & \dots & \Delta V_{1j}^{t} & \Delta V_{1j+1}^{t} & \dots & \Delta V_{mkt} \\ \vdots & \vdots & \vdots & \vdots & \vdots & \vdots & \vdots & \vdots \\ \Delta V_{i1}^{t} & \dots & \Delta V_{ip}^{t} & \dots & \Delta V_{ij}^{t} & \Delta V_{ij+1}^{t} & \dots & \Delta V_{ik}^{t} \\ \Delta V_{i+11}^{t} & \dots & \Delta V_{i+1p}^{t} & \dots & \Delta V_{i+1j}^{t} & \Delta V_{i+1j+1}^{t} & \dots & \Delta V_{i+1k}^{t} \\ \vdots & \vdots & \vdots & \vdots & \vdots & \vdots & \vdots & \vdots \\ \Delta V_{q1}^{t} & \dots & \Delta V_{qp}^{t} & \dots & \dots & \dots & \dots & \Delta V_{qk}^{t} \\ \vdots & \vdots & \vdots & \vdots & \vdots & \vdots & \vdots & \vdots \\ \Delta V_{m1}^{t} & \dots & \Delta V_{mp}^{t} & \dots & \Delta V_{mj}^{t} & \Delta V_{mj+1}^{t} & \dots & \Delta V_{mk}^{t} \end{bmatrix} \quad (15)$$

where ΔV_{ij}^{t} refers to change in voltage at the sensing coil located at position (i, j), between time $t-1$ and t. Furthermore, the negative and positive signs of ΔV_{ij}^{t} determine the direction of motion. As shown in Fig. 11, if an object is moving toward the center of sensing coil, the voltage changes are positive, and negative if it is moving away. This means the direction of motion is always from negative ΔV to positive. To demonstrate this, Fig. 10 shows two objects (i.e., phone and laptop) moving from time $t-1$ to t and then to $t+1$. The corresponding voltage gradient matrix can be calculated as follows:

$$\Delta V(t-1,t) = \begin{bmatrix} 0 & 0 & 0 & \Delta V_{14}^{t}(-) & \Delta V_{15}^{t}(-) & \Delta V_{16}^{t}(-) \\ \Delta V_{21}^{t}(+) & 0 & 0 & \Delta V_{24}^{t}(-) & \Delta V_{25}^{t}(-) & \Delta V_{26}^{t}(-) \\ \Delta V_{31}^{t}(+) & 0 & \Delta V_{33}^{t}(+) & \Delta V_{34}^{t}(+) & \Delta V_{35}^{t}(+) & 0 \\ \Delta V_{41}^{t}(-) & 0 & \Delta V_{43}^{t}(+) & \Delta V_{44}^{t}(+) & \Delta V_{45}^{t}(+) & 0 \\ 0 & 0 & 0 & 0 & 0 & 0 \\ 0 & 0 & 0 & 0 & 0 & 0 \end{bmatrix} \quad (16)$$

$$\Delta V(t,t+1) = \begin{bmatrix} 0 & 0 & 0 & 0 & 0 & 0 \\ \Delta V_{21}^{t+1}(-) & \Delta V_{22}^{t+1}(+) & 0 & 0 & 0 & 0 \\ \Delta V_{31}^{t+1}(-) & \Delta V_{32}^{t+1}(+) & \Delta V_{33}^{t+1}(-) & \Delta V_{34}^{t+1}(-) & \Delta V_{35}^{t+1}(-) & 0 \\ 0 & 0 & \Delta V_{43}^{t+1}(-) & \Delta V_{44}^{t+1}(-) & \Delta V_{45}^{t+1}(-) & 0 \\ 0 & 0 & \Delta V_{53}^{t+1}(+) & \Delta V_{54}^{t+1}(+) & \Delta V_{55}^{t+1}(+) & 0 \\ 0 & 0 & \Delta V_{63}^{t+1}(+) & \Delta V_{64}^{t+1}(+) & \Delta V_{65}^{t+1}(+) & 0 \end{bmatrix}. \quad (17)$$

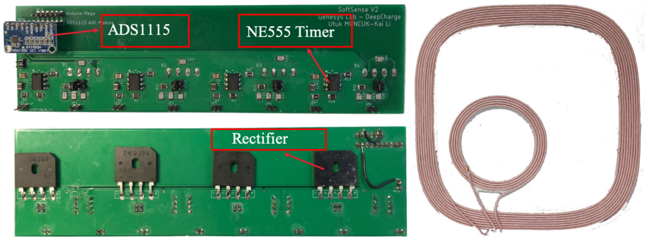

(a) (b)

Fig. 12. iSense node (a) fabricated PCB board and (b) fabricated dual-coil.

Here, motion vectors are determined based on the indicated signs, from negative to positive.

IV. iSENSE HARDWARE IMPLEMENTATION

This section discusses the details of iSense hardware implementation, including the dual coil design, waveform generator, microcontroller, and the choice of the components selection. Fig. 12 shows components of our proposed low-power iSense nodes, which consists of four identical individual iSense node, each node connect one dual-coil. Each node consists of three main subunits: 1) a waveform generator; 2) an analog-digital converter (ADC); and 3) a rectifier. The waveform generator generates low-power square-wave signal at 200 kHz and applies it to the sensing coil. The dual-coil sensing configuration has subcoils of two different size and shape. The inner coil is connected in serial with a capacitor and then linked to a waveform generator to generate a magnetic field by resonating at 200 kHz. The voltage rectifier converts the ac voltage at the outer coil into functional dc voltage. The presence of an object within the sensing coil coverage causes the voltage drop at the output of voltage rectifier. The ADC converts this voltage drop at the output of the voltage rectifier into the digital format and recorded by microcontroller. Fig. 12(a) shows the fabricated printed circuit board (PCB) of the iSense multichannel prototype with front view and back view. This prototype has four sensing channels, where each channel includes one wave generator based on the NE555 timer, and one rectifier based on the ON semiconductor full-bridge GBU8JFS-ND. The voltage changes at output of these rectifiers are recorded in real-time by the ADC. We utilize an ARM-cortex microcontroller that processes digital data generated by ADC and performs the classification and tracking algorithms. We design the PCB board in two layers, one of which serves as a ground plane and fabricate it with an FR-4 epoxy glass substrate.

We use one group coils configuration consisting of eight sensing nodes covering around 25 cm × 50 cm surface area where each node has coil size 12 cm × 12 cm to conduct the experiments in Section V. Fig. 12(b) shows this fabricated dual-coil made of litz wire with 1.15-mm diameter. It is same as the wire used in the state-of-the-art Qi standard. Additionally, we use two-group configuration consisting of six sensing nodes that cover around 29 cm×44 cm surface area with group one coil size 14.5cm×14.5cm and group two coil size 12 cm×12 cm to conduct the experiments in Section VI for the mobile robot car application.

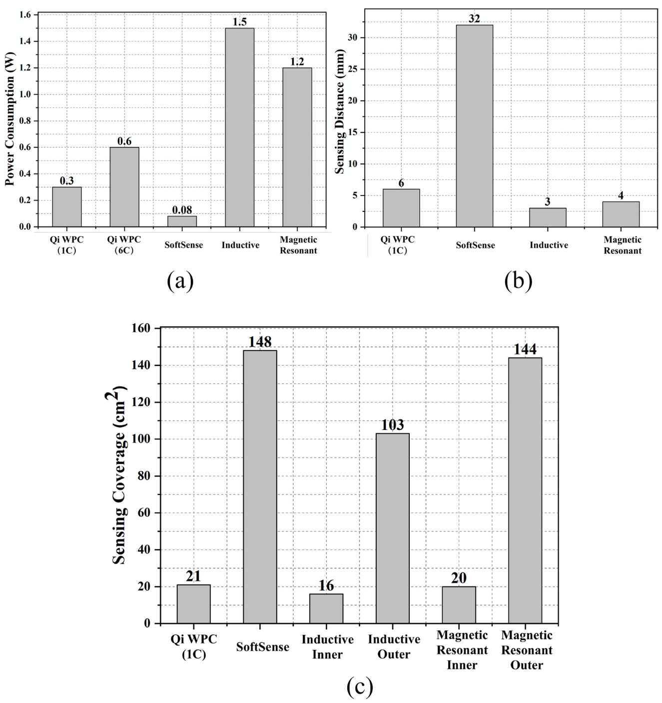

Fig. 13. Sensing performance comparison in terms of (a) power consumption, (b) sensing distance, and (c) sensing coverage.

V. Experimental Results

In this section, we first evaluate the performance of our magnetic contactless sensing with other coil-based state-of-the-art techniques, and then study the ability to detect objects, identify their types, and track motion and direction of the movement.

Fig. 13(a) compares power consumption between *inductive sensing* via a coil of the same size of the outer iSense coil connected to the wave generator, and *magnetic resonance sensing* consisting, again with the same coil size and a resonant capacitor connected to a wave generator. We set the sensing range up to 3 cm for the purpose of comparison. Here, the energy consumption includes microcontroller, circuit and coil energy consumption. Additionally, we compare them with Qi (i.e., WPC standard version 1.2) for two Qi configurations: 1) one sensing coil that results in 12% sensing area of a iSense node and 2) six overlapping coils that provide same sensing area as the iSense node. We observe that iSense consumes 18.5× less than the inductive sensing, 15× less than magnetic resonance sensing, 7.5× less than Qi with six coils, and 3.75× less than Qi with one coil. Fig. 13(b) compares sensing distance between Qi, inductive sensing, magnetic sensing, and iSense. Here, sensing distance is set as the maximum distance that a phone can be detected with 95% accuracy. Thus, iSense significantly outperforms other techniques with more than 5× margin. Fig. 13(c) depicts the sensing coverage and considers two sensing configurations for each of inductive and magnetic resonance sensing. We vary the coil dimensions to match the smaller inner iSense active coil, and also to match the size of the outer coil. We see that iSense provides the highest sensing coverage compared to other methods. Next, we evaluate the performance of iSense to identify the type of objects based on the measured voltage change. We train and test our classifier for seven objects with different sizes and shapes, such as phone (iPhone X), laptop (Acer TravelMate X3), mouse (Logitech wireless mouse m275), metal plate (size 7 cm × 7 cm and thickness of 1 mm), game controller (Xbox wireless controller), tablet (iPad), and power adapter (Belker 70 w laptop charger).

TABLE II
Voltage Changes for Different Models of Laptop, Phone, and Tablet

Device Type	Model	Voltage Change (mV)
Laptop	Acer Travel Mater X3	720mV
	Macbook Air	790mV
	AlienWare M15	760mV
Phone	iPhone X	410mV
	Huawei P30 Pro	420mV
Tablet	iPad	510mV
	Surface Pro 5	540mV

We run iSense on a Teensy 3.2 board that has an ARM-cortex microcontroller with TensorFlow Lite requiring only kilobytes of memory to load and run the SVM classifier [32]. We conduct a total of 150 experiments for each type of object. The Teensy board collects data with a sampling rate of 20 ms for the duration of 5 s in each experiment. We log and store the sensing data from Teensy to an external computer via USB in the training stage and then train the classifier offline. We then load the trained classifier into the microcontroller for real-time device type detection using Tensorflow Lite. The classifier takes 5 s for object type inference.

The nodes are placed on three over-the-surface materials: 1) a large wooden conference table; 2) a coffee shop table with hybrid wood composition; and 3) a library table with hard plastic. The nodes are placed at distance 3 cm from each other, ensuring full sensing coverage of the surface.

Fig. 14(a) shows the average measured voltage changes for different object types when placed in the center of the coil and repeated ten times for each material. We see all three materials have a negligible impact of less than 15 mV on the average voltage change and that regardless of surface materials, different objects introduce distinguishable variations in the voltage. It is noteworthy that voltage readings can have errors of 10–15 mV due to eddy current errors [33] and ADC reading errors [34], such as analog-signal source resistance, analog-input signal noise, and ADC dynamic range change on the sensing signal and, thus, such small changes that can be observed in Fig. 14(a) due to surface materials consider negligible. On the other hand, Fig. 14(b) shows the results for detection accuracy at different sensing distances for the object type phone. It indicates 3 cm as the effective sensing distance here, which is similar for other object types.

Table II shows the measured voltage changes of three different models for laptops, two different models for phone, and two different models for tablet. It can be observed that the voltage changes of different models for the same type create similar clusters of values and validate the practicality of our classification approach on detecting the type of devices from different manufacturers' models. Additionally, it can be observed that MacBook Air has the highest voltage change

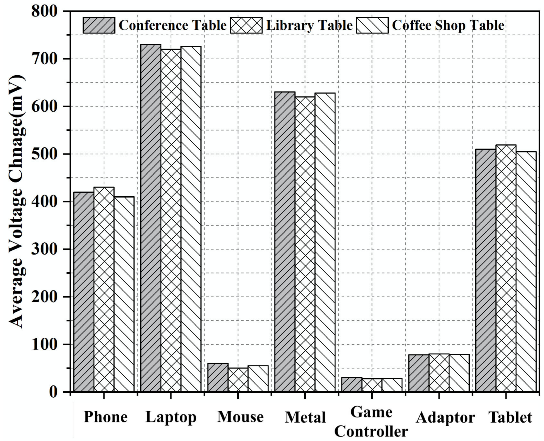

(a)

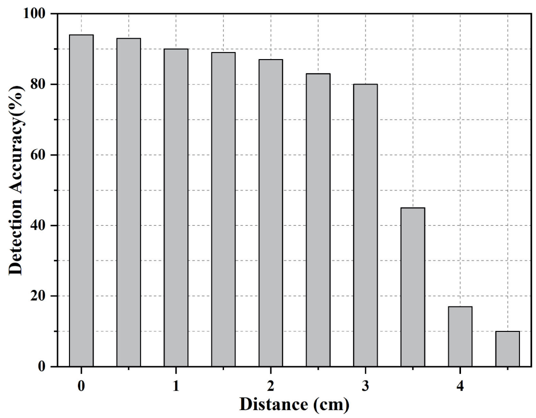

(b)

Fig. 14. (a) Average voltage change for different objects and three over-surface materials. Object detection accuracy for (b) phone, and different sensing distances.

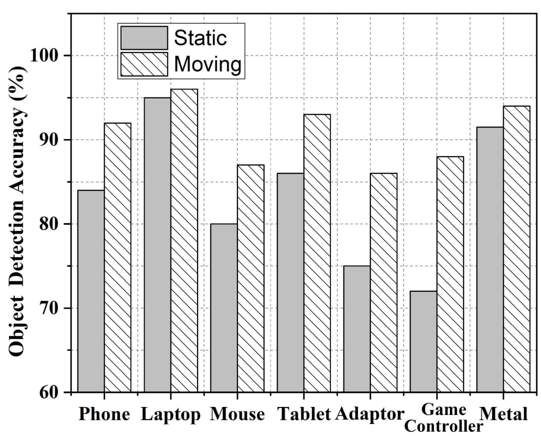

Fig. 15. Static and moving object detection accuracy for different types of objects.

due to its aluminum alloy shell, even though it has a smaller size. On the other hand, Huawei P30 Pro and Surface Pro 5 have bigger sizes than iPhone X and iPad, resulting in higher voltage changes.

Finally, Fig. 15 presents the results for static objection detection accuracy and moving object detection accuracy for different object types at the fixed sensing distance 3 cm. ADC errors that result in more than 100-mV voltage change are enough to swap the signs of estimations in the voltage gradient from positive to negative or *vice versa*, which leads to misdetection. Despite such errors, Fig. 15 indicates the high accuracy of iSense object tracking. Here, a key to device detection accuracy is higher and more frequent voltage changes in the presence of ADC errors, eddy errors, and weak magnetic fields. As the device is moving, the voltage change samples are obtained from readings of multiple sensing nodes over the surface, while for a static object, they are obtained from the same node and no physical object change over the sensing coil. Accordingly, for moving object detection, the variance in the voltage change is much higher than that in the case of a static object.

In the future, we plan to explore the use of more advanced machine learning models, such as convolutional neural networks (CNN) for object classification. Additionally, we will investigate increasing the sensing distance by having multiple levels of inner nested coils, and building experimental works on sensing additional hardware models for each type of device.

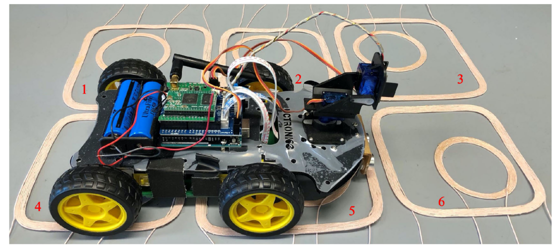

Fig. 16. iSense-based robot car localization and tracking over a larger surface with multiple different size of coils.

VI. Application: Mobile Robot Car

In this section, we present an application of our networked sensing system for a mobile robot car and evaluate its performance in terms of 1) interference mitigation over surface sensing; 2) car sensing voltage change patterns; 3) car localization and tracking; and 4) car velocity estimation.

Fig. 16 shows our real-time mobile car tracking prototype. We use sensing coils with dual-coil design layout and two different size configurations (l_1 and l_2), where each size corresponds to a sensing group, as discussed in interference mitigation section. In the example case of six sensing coils, three coils are assigned as group one and three coils as group two. The group one coils have a size of 14.5 cm $\times$ 14.5 cm, and 12 cm $\times$ 12 cm is for group two, and the gap between the larger coil and the smaller coil is 1.5 cm. To reduce the parasitic resistance effect of coil, we use Litz wire with low pure resistance, and we utilize an UCTRONICS WIFI smart car [35] as mobile object with dimension of 15 cm $\times$ 25 cm and a height of 2 cm from chassis to the coil surface. We customize this car by adding metallic material for increasing the object detection sensitivity in presence of the magnetic field. The sensing surface with the multiple coils are located at the laboratory desk that is made of wood.

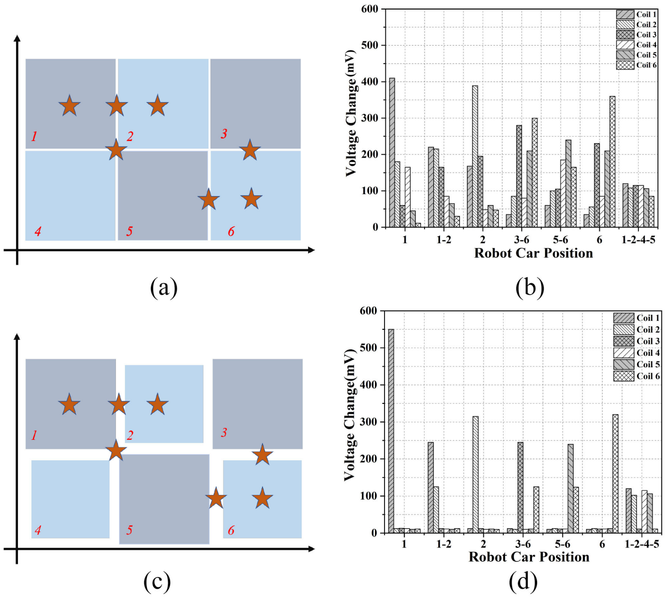

Fig. 17. (a) One sensing group with different center positions of the car indicated with stars. (b) Coupling interference-induced voltage changes for configuration of one sensing group. (c) Two sensing groups with different center positions of the car that are indicated with star. (d) Comparison of voltage changes for configuration of two sensing groups.

To estimate the direction of the moving object, we use the gradient matrix-based estimation as explained in Section III. In our experiment, we assume the sensing input reading rate is n_{bit}bit/s, the robot car speed is v_{car}, and the car speed is less than the reading rate through the whole experiment. When the robotic car travels a certain distance l with the total m_{bit} number of sensing samples, the car speed can be calculated as

$$v_{car} = l/t, \quad \text{where} \quad t = m_{\text{bit}}/n_{\text{bit}}. \tag{18}$$

Fig. 17(a) and (c) depicts the sensing surface configuration for example of six coils where Fig. 17(a) shows the case of equal size coils, Fig. 17(b) shows the case of two sensing groups, and each sensing coil is labeled from one to six. The stars represent seven examples for center position of the robot car. The car can overlap with one, two, three, and four sensing coils depending on its location.

Fig. 17(b) and (d) shows the results of voltage change when the robot car is located at these seven starred locations over the surface. Here, "1" means car is located at sensing coil 1, and 1-2, 3-6, 5-6, 1-2-4-5 represent coil numbers that are covered by car in each case. Additionally, at each car position, the voltage changes for all six coils measured at the same time. It can be observed in both cases when the sensing coils are covered fully or partially with the car, there are clear voltage changes, such as 550, 320, 225, 120, 100 mV for Fig. 17(d). On the other hand, Fig. 17(d) shows for the case of group-based coil layout, where the sensing coils do not experience any changes (0 mV) due to coupling interference mitigation. Fig. 17(b) shows the case of equal-size coils, where all coils experience significant coupling interference. Our results reveal that by comparing the coil voltage change, we can deduce the location of the robot car. For instance, at position 1, only first sensing coil provides clear voltage changes that are bigger than other coils. Same approach applies to example positions 3-6 and 1-2-4-5, where based on the voltage change of each coil, we can estimate the location of car between coil 3 and coil 6 and in the center with coils 1, 2, 4, and 5.

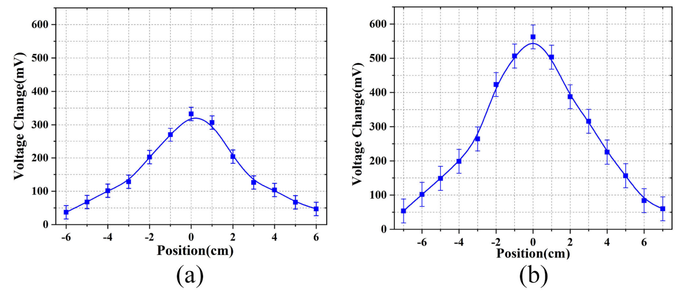

Fig. 18. Voltage change for different positions on (a) coil 2 and (b) coil 3.

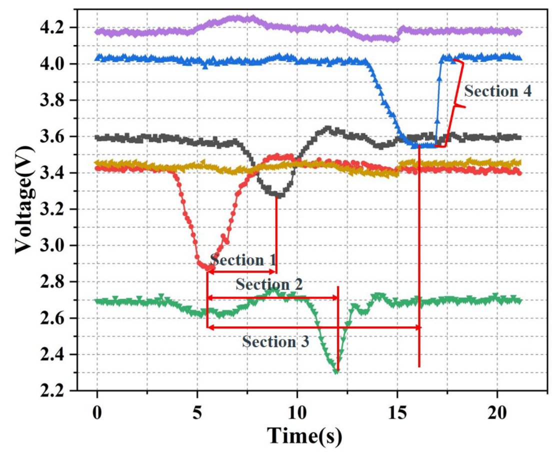

Fig. 19. Time-series of the voltage change for six sensors while the mobile car is moving.

Next, we record the voltage changes for two sensing group configurations and for each 1 cm moving resolution when the robot car moves slightly over an individual sensing coil. Fig. 18 demonstrates the minimum voltage change that is induced due to the presence on the car on the sensing coil. This value is 50 mV, much greater than the coupling interference from neighbor coils [Fig. 17(d)]. Additionally, we observe that voltage change increases when the car moves into center and decreases when the car moves out of the coil by comparing the value change between two continue time "t" and "$t + 1$." Thus, the direction of the car can be determined as moving toward the center or away from it.

Finally, we conduct a set of the experiments to evaluate the performance of tracking and velocity estimation. As shown in Fig. 16, the robotic car moves along sensing coils: coil 1 $\rightarrow$ coil 2 $\rightarrow$ coil 3 $\rightarrow$ coil 6. Fig. 19 presents the time series of voltage changes at all coils while the robot car is moving. We observe that the combined voltage change patterns of all sensors determine the location and direction of movement. For example, from moment $t = 5$ s to moment $t + 1 = 6$ s, the voltage change in coil 1 keeps going down, which means that the robot car is moving out the coil. At the same time, the voltage change of coil 2 (black curve) goes up, which means that the robot car is moving toward the center of sensing coil 2.

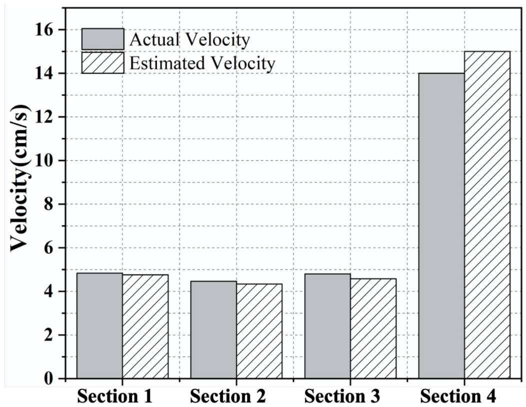

Fig. 20. Comparison between the actual and estimated velocities of the robot car.

Combining the voltage change of these two coils, the location and the moving direction of the robot is determined as from coil 1 → coil 2. Second, the moving velocity is estimated according to the voltage change. The robot car can move over the surface with different velocities.

To evaluate the performance and accuracy of our velocity estimation with the actual velocity, we divide the moving distance into four sections with section 1: coil 1 → coil 2, section 2: coil 1 → coil 3, section 3: coil 1 → coil 6, and section 4: car moving out of coil 6 with faster actual velocity as seen in Fig. 19. For all the four sections, the distance is measured from the center to center and from the center to the edge. Based on the size of the whole coil surface and the car size, the experiment continues around 20 s as shown in Fig. 19. In the experiment, we calculate the moving time by taking into account how many data are recorded and then estimate the car velocity based on (18). Fig. 20 shows the comparison between actual velocity and the estimated velocity among these four sections and demonstrates that estimated velocity is more than 90%. Furthermore, the system can distinguish different velocities; for example, the car velocity at section 4 is much faster than sections 1–3, as the robot car move quickly out from coil 6 but moves slowly from the center of coil 1 to the center of coil 6.

VII. Conclusion

This article introduced a contactless magnetic sensing system with dual-coil configuration, with one coil as the driving loop and the other as a passive coil that acts as a resonator relay. This configuration can extend the sensing distance to 3–4 cm using a 200-KHz ac signal source. The sensing system can robustly distinguish objects, such as a phone, laptop, metals, and mouse based on their voltage change with 94% accuracy and localize the position of the phone with cm accuracy. Our sensing experiments on object tracking reveal 96% accuracy, with a total energy cost of 80 mW in each of these scenarios. We demonstrated an application for the localization and tracking of a robot mobile car and estimated its moving direction and moving velocity. The experimental results showed that the interference between coils due to the mutual inductance can be removed by using coil size grouping. Furthermore, our experiments revealed the mobile care velocity estimation with more than 90% accuracy.

References

[1] M. Y. Naderi, K. R. Chowdhury, and S. Basagni, "Wireless sensor networks with RF energy harvesting: Energy models and analysis," in *Proc. IEEE Wireless Commun. Netw. Conf. (WCNC)*, 2015, pp. 1494–1499.

[2] H. Kharrufa, H. A. Al-Kashoash, and A. H. Kemp, "RPL-based routing protocols in IoT applications: A review," *IEEE Sensors J.*, vol. 19, no. 15, pp. 5952–5967, Aug. 2019.

[3] A. Triantafyllou, P. Sarigiannidis, and T. D. Lagkas, "Network protocols, schemes, and mechanisms for Internet of Things (IoT): Features, open challenges, and trends," *Wireless Commun. Mobile Comput.*, vol. 2018, Sep. 2018, Art. no. 5349894.

[4] A. Jaddoa, G. Sakellari, E. Panaousis, G. Loukas, and P. G. Sarigiannidis, "Dynamic decision support for resource offloading in heterogeneous Internet of Things environments," *Simulat. Model. Pract. Theory*, vol. 101, May 2020, Art. no. 102019.

[5] H.-P. Lin, C.-Y. Jung, T.-Y. Huang, H. Hendrick, and Z.-H. Wang, "NB-IoT application on decision support system of building information management," *Wireless Pers. Commun.*, vol. 114, pp. 711–729, Apr. 2020.

[6] L. Chen *et al.*, "Range extension of passive wake-up radio systems through energy harvesting," in *Proc. IEEE Int. Conf. Commun. (ICC)*, 2013, pp. 1549–1554.

[7] J. Xiong and K. Jamieson, "Arraytrack: A fine-grained indoor location system," in *Proc. 10th USENIX Symp. NSDI*, Lombard, IL, USA, 2013, pp. 71–84.

[8] X. Guo, N. R. Elikplim, N. Ansari, L. Li, and L. Wang, "Robust WiFi localization by fusing derivative fingerprints of rss and multiple classifiers," *IEEE Trans. Ind. Informat.*, vol. 16, no. 5, pp. 3177–3186, May 2020.

[9] D. Bharadia, K. R. Joshi, M. Kotaru, and S. Katti, "BackFi: High throughput WiFi backscatter," *ACM SIGCOMM Comput. Commun. Rev.*, vol. 45, no. 4, pp. 283–296, 2015.

[10] U. Ha, Y. Ma, Z. Zhong, T.-M. Hsu, and F. Adib, "Learning food quality and safety from wireless stickers," in *Proc. 17th ACM Workshop Hot Topics Netw.*, 2018, pp. 106–112.

[11] Z. Luo, Q. Zhang, Y. Ma, M. Singh, and F. Adib, "3D backscatter localization for fine-grained robotics," in *Proc. 16th USENIX Symp. NSDI*, Boston, MA, USA, 2019, pp. 765–782.

[12] *Wireless Power Consortium*. (2020). [Online]. Available: https://www.wirelesspowerconsortium.com/qi/

[13] J. Sundeen and R. Buchanan, "Thermal sensor properties of cermet resistor films on silicon substrates," *Sens. Actuators A, Phys.*, vol. 90, nos. 1–2, pp. 118–124, 2001.

[14] L. E. Aygun *et al.*, "Large-area resistive strain sensing sheet for structural health monitoring," *Sensors*, vol. 20, no. 5, p. 1386, 2020.

[15] Y. Zhang, G. Laput, and C. Harrison, "Electrick: Low-cost touch sensing using electric field tomography," in *Proc. CHI Conf. Human Factors Comput. Syst.*, 2017, pp. 1–14.

[16] T. Grosse-Puppendahl *et al.*, "Finding common ground: A survey of capacitive sensing in human-computer interaction," in *Proc. CHI Conf. Human Factors Comput. Syst.*, 2017, pp. 3293–3315.

[17] L. Xiang, Z. Zhu, J. Tian, and Y. Tian, "Foreign object detection in a wireless power transfer system using symmetrical coil sets," *IEEE Access*, vol. 7, pp. 44622–44631, 2019.

[18] S.-J. Huang, J.-L. Su, S.-H. Dai, C.-C. Tai, and T.-S. Lee, "Enhancement of wireless power transmission with foreign-object detection considerations," in *Proc. IEEE 6th Glob. Conf. Consum. Electron. (GCCE)*, 2017, pp. 1–2.

[19] B. Cheng, J. Lu, Y. Zhang, G. Pan, R. Chabaan, and C. C. Mi, "A metal object detection system with multilayer detection coil layouts for electric vehicle wireless charging," *Energies*, vol. 13, no. 11, p. 2960, 2020.

[20] D. Patil, J. M. Miller, B. Fahimi, P. T. Balsara, and V. Galigekere, "A coil detection system for dynamic wireless charging of electric vehicle," *IEEE Trans. Transp. Electrification*, vol. 5, no. 4, pp. 988–1003, Dec. 2019.

[21] S. Y. Jeong, V. X. Thai, J. H. Park, and C. T. Rim, "Metal object detection system with parallel-mistuned resonant circuits and nullifying induced voltage for wireless EV chargers," in *Proc. Int. Power Electron. Conf. (IPEC-Niigata-ECCE Asia)*, 2018, pp. 2564–2568.

[22] S. Y. Chu and A.-T. Avestruz, "Electromagnetic model-based foreign object detection for wireless power transfer," in *Proc. 20th Workshop Control Model. Power Electron. (COMPEL)*, 2019, pp. 1–8.
[23] K. Li, U. Muncuk, M. Y. Naderi, and K. R. Chowdhury, "SoftSense: Collaborative surface-based object sensing and tracking using networked coils," in *Proc. IEEE Glob. Commun. Conf. (GLOBECOM)*, 2019, pp. 1–6.
[24] L.-X. Chuo, Z. Luo, D. Sylvester, D. Blaauw, and H.-S. Kim, "RF-Echo: A non-line-of-sight indoor localization system using a low-power active RF reflector ASIC tag," in *Proc. MobiCom*, 2017, pp. 222–234.
[25] J. Jadidian and D. Katabi, "Magnetic MIMO: How to charge your phone in your pocket," in *Proc. ACM Mobicom*, 2014, pp. 495–506.
[26] A. Kurs, A. Karalis, R. Moffatt, J. D. Joannopoulos, P. Fisher, and M. Soljačić, "Wireless power transfer via strongly coupled magnetic resonances," *Science*, vol. 317, no. 5834, pp. 83–86, Jul. 2007.
[27] B. H. Waters, B. J. Mahoney, G. Lee, and J. R. Smith, "Optimal coil size ratios for wireless power transfer applications," in *Proc. IEEE Int. Symp. Circuits Syst. (ISCAS)*, 2014, pp. 2045–2048.
[28] S. R. Khan, S. K. Pavuluri, and M. P. Y. Desmulliez, "Accurate modeling of coil inductance for near-field wireless power transfer," *IEEE Trans. Microw. Theory Techn.*, vol. 66, no. 9, pp. 4158–4169, Sep. 2018.
[29] Y. Cheng and Y. Shu, "A new analytical calculation of the mutual inductance of the coaxial spiral rectangular coils," *IEEE Trans. Magn.*, vol. 50, no. 4, Apr. 2014, Art. no. 7026806.
[30] *COMSOL Multiphysics*. (2020). [Online]. Available: https://www.comsol.com
[31] *Analogy Discovery*. (2020). [Online]. Available: https://analogdiscovery.com
[32] *TensorFlow Lite*. (2020). [Online]. Available: https://www.tensorflow.org/lite/microcontrollers
[33] S. J. Norton and J. R. Bowler, "Theory of eddy current inversion," *J. Appl. Phys.*, vol. 73, no. 2, pp. 501–512, 1993.
[34] Freescale Semiconduct., Austin, TX, USA, Capacitor tolerance, (2016). [Online]. Available: https://www.nxp.com/docs/en/application-note/AN5250.pdf
[35] *Robot Car*. (2020). [Online]. Available: https://www.uctronics.com

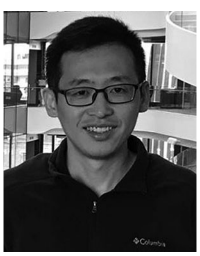

Kai Li (Student Member, IEEE) received the B.S. degree in applied physics and the M.S. degree in physics from Qingdao University, Shandong, China, in 2014 and 2017, respectively. He is currently pursuing the Ph.D. degree in electrical engineering under the guidance of Prof. K. R. Chowdhury with Northeastern University, Boston, MA, USA.

His research interests include design, optimization and implementation for wireless power transfer circuits, analysis of electromagnetic field in near field, system design for magnetic resonant coupling-based networked coil sensing, lower-power to high-power amplifier circuit design, analog and digital circuit design, and wireless mesh networks communication.

Mr. Li was a recipient of Best Paper Awards at IEEE GLOBECOM in 2019.

Ufuk Muncuk received the Ph.D. degree in electrical and computer engineering from Northeastern University, Boston, MA, USA, in 2019.

He is a Research Assistant Professor with the Electrical and Computer Engineering Department, Northeastern University. His research interests include design, optimization, and implementation for RF energy harvesting circuits, use of wireless energy transfer, system design for joint RF energy and magnetic coupling-based energy transfer, system design for intrabody transceivers, analog and digital circuit design, wireless sensor networks, and cognitive radio systems.

Dr. Muncuk was a recipient of the Best Paper Runners-Up at ACM SenSyS in 2018, and the Best Paper Awards at IEEE ICC in 2013, and IEEE GLOBECOM in 2019.

M. Yousof Naderi received the Ph.D. degree in electrical and computer engineering from Northeastern University, Boston, MA, USA, in 2015.

He is a Research Assistant Professor with the Electrical and Computer Engineering Department, Northeastern University. His research expertise lies in the design and development of software-defined wireless systems, wireless energy transfer and harvesting, and AI-enabled embedded solutions for next-generation cyber–physical systems. In the above areas, he has coauthored numerous scientific journal and conference paper publications, served as reviewer for more than hundred papers in journals and conferences, and TPC and organizer of several academic conferences and workshops.

Dr. Naderi was a recipient of the NEU Ph.D. Dissertation Award in 2015, the Finalist in the Bell Labs Prize Competition in 2017, and the Best Paper Awards at the IEEE INFOCOM in 2018, and IEEE GLOBECOM in 2019.

Kaushik R. Chowdhury (Senior Member, IEEE) received the M.S. degree from the University of Cincinnati, Cincinnati, OH, USA, in 2006, and the Ph.D. degree from the Georgia Institute of Technology, Atlanta, GA, USA, in 2009.

He was an Assistant Professor from 2009 to 2015, and an Associate Professor from 2015 to 2020 with Northeastern University, Boston, MA, USA, where he is currently a Professor with the Electrical and Computer Engineering Department. His current research interests include deep learning in wireless networks, wireless RF energy harvesting, and IoT and in the area of intra/on-body communication.

Prof. Chowdhury was a Winner of the Presidential Early Career Award for Scientists and Engineers in 2017, the ONR Director of Research Early Career Award in 2016, and the NSF CAREER Award in 2015.